Effect of impulsive transient electric fields on autoionization

J. G. Zeibel, S. N. Pisharody, and R. R. Jones
Department of Physics, University of Virginia, Charlottesville, Virginia 22904
(Received 11 October 2002; published 29 January 2003)

Picosecond half cycle pulses (HCPs) have been used to examine the effect of transient electric fields on the autoionization of doubly excited states of calcium. The autoionization yield, following picosecond isolated core excitation (ICE) of $4pnd$ Rydberg states, has been measured as a function of the relative delay between the transient field and the ICE laser pulse. Using single and multiple HCPs in combination with a static electric field, we explicitly investigate the relative importance of static field induced ℓ mixing, and transient field excitation of high-ℓ, low-m or high-ℓ, high-m states on the suppression of autoionization. Our experimental results can be understood using semiclassical analyses and are well reproduced by quantum simulations.

DOI: 10.1103/PhysRevA.67.013409 PACS number(s): 32.80.Rm, 34.80.Lx

I. INTRODUCTION

A number of internal conversion processes in Rydberg atoms and molecules are mediated by energy transfer between a Rydberg electron and the multiparticle, ionic core to which it is bound [1–4]. During autoionization (AI), a bound Rydberg electron is promoted to the continuum during a superelastic collision with an energetically excited core. The first stage of dielectronic recombination (DR), the capture of a continuum electron into a bound autoionizing state, is the precise inverse of autoionization. The second step in DR is the stabilization of the autoionizing state via spontaneous emission or inelastic collisional deexcitation [1–3]. In predissociation (PD), a Rydberg electron bound to a stable molecular ion undergoes resonant collisional energy transfer with the ion core, resulting in dissociation of the molecule. The rates for all of these processes depend critically on the overlap of the Rydberg wave function with the compact ion core. This overlap decreases with increasing values of principal and angular-momentum quantum numbers, n and ℓ, for the Rydberg electron [5]. For constant ℓ, the probability for finding the Rydberg electron in the vicinity of the ion core scales as n^{-3}, in inverse proportion to the electron's classical Kepler period, $\tau_K = 2\pi n^3$ (unless otherwise noted, atomic units are used throughout). For constant n there is no simple ℓ scaling formula. The electron-ion core overlap is relatively constant for low-ℓ states due to the finite size of the ion core. However, the overlap decreases extremely rapidly with increasing ℓ due to the centrifugal barrier at small electron radius. Typically, for $\ell \gtrsim 3$, the ion core is localized well within the radial volume $r \lesssim \ell(\ell+1)/2$ that is classically forbidden to the Rydberg electron [5,6]. Consequently, for these high-ℓ states the AI, DR, and PD rates drop precipitously with increasing ℓ, and are considerably smaller than the corresponding rates of the low-ℓ ($\lesssim 3$) states [7–10].

Not surprisingly, externally applied fields that affect the angular-momentum composition of the Rydberg wave function, can have a dramatic influence on AI, PD, and DR rates. Consider the case of a uniform static electric field. In the presence of the field, the potential that binds the Rydberg electron no longer possesses (near) spherical symmetry and, therefore, electronic angular momentum is no longer a conserved quantity. However, m, the quantum number corresponding to the projection of the electron's angular momentum on the field axis, remains good in the field [5,6]. For each principal quantum number n and angular-momentum projection m, there are $n-m$ ''Stark'' states which are linear combinations of the available $n-m$ angular-momentum eigenstates [11]. To a rough approximation, all of the $n-m$ Stark states corresponding to a specific n,m Stark manifold, share single average AI, PD, or DR rates, Γ_{AI_S}, Γ_{PD_S}, or Γ_{DR_S}, respectively. Each Γ_S is simply the average of the respective process rates for the constituent ℓ states ($m \leqslant \ell < n$) in each Stark level [12–15]. Moreover, because the large core-scattering rates for the lower ℓ states dominate the average, in low-m ($\lesssim 4$) manifolds the AI and PD rates are a factor of order of $1/n$ smaller than the corresponding rate for a pure $\ell \sim m$ level. Typically, due to dipole selection rules, states that can be reached by purely optical excitation have low m. Consequently, in a sufficiently strong static field [16], AI and PD rates of angularly mixed Stark states are *suppressed* by a factor $\sim 1/n$ relative to the pure levels that are optically accessible in zero field [12–15].

DR is also affected by angular-momentum mixing, but the observed rates are *enhanced* rather than suppressed by the field [15,17–22]. To understand this, consider an atomic system with doubly excited levels that decay through autoionization or are stabilized via spontaneous emission to nonautoionizing states. The contribution of a single autoionizing state, $|\ell\rangle$ to the total dielectronic recombination rate Γ_{DR} is equal to the rate at which a continuum electron is captured into state $|\ell\rangle$ multiplied by the branching ratio for decay of $|\ell\rangle$ by spontaneous emission rather than autoionization [13,20–23],

$$\Gamma_{DR_\ell} = \beta \Gamma_{AI_\ell} \frac{\gamma}{\Gamma_{AI_\ell} + \gamma}, \tag{1}$$

where β is a constant numerical factor, Γ_{AI_ℓ} is the AI rate of a pure ℓ state, and γ is the spontaneous emission rate. For doubly excited Rydberg states, γ is often dominated by emission from the core and, therefore, is ℓ independent. For low ℓ, Γ_{AI_ℓ} is typically several orders of magnitude greater than γ, while for high ℓ, Γ_{AI_ℓ} can be several orders of magnitude

smaller than γ [10]. Since Γ_{AI_ℓ} decreases rapidly with increasing ℓ, to a good approximation $\Gamma_{AI_\ell} \neq \gamma$ for any ℓ, and Eq. (1) reduces to

$$\Gamma_{DR_\ell} \approx \beta \Gamma_{AI_\ell}, \quad \ell \geqslant \ell_c, \tag{2}$$

and

$$\Gamma_{DR_\ell} \approx \beta\gamma, \quad \ell < \ell_c, \tag{3}$$

where ℓ_c is the critical value of ℓ for which $\Gamma_{AI_\ell} = \gamma$. Because $\Gamma_{AI_{\ell > \ell_c}}$ is typically many orders of magnitude smaller than γ, states with $\ell > \ell_c$ contribute little or nothing to the total DR rate, and the total DR rate is proportional to γ multiplied by the number of states N with $\ell < \ell_c$. Therefore, for large principal quantum number $n \gg \ell_c$, only a small fraction of the total number of pure $n\ell$ states in zero field can contribute to DR. However, as discussed in the preceding paragraph, angular momentum mixing in a static field homogenizes the AI rate over each Stark level in a given n manifold. For the low m states that contribute to DR, all states in the Stark manifold autoionize at a rate much greater than the spontaneous emission rate. Consequently, *every* Stark state contributes an additive factor of $\beta\gamma$ to the total DR rate, thereby enhancing the DR contribution from each n manifold by a factor of $\approx n/\ell_c$ [9,21]. The effect of the static field is to convert pure ℓ states that do not contribute to DR into Stark states that do.

Not surprisingly, analogous ℓ mixing, AI suppression of optically accessible states, and the enhancement of DR also occur if the static field is replaced by a uniform, linearly polarized rf, or low-frequency microwave field [4,13,24]. Here, low frequency is defined as a frequency less than the the energy splitting $\Delta E \approx n^{-3}$, between adjacent n states at the excitation energy of interest. The situation is dramatically different, however, if: (i) the rf field has a time-dependent polarization [23,25]; (ii) the static or rf electric field is applied in the presence of a strong static magnetic field with a noncolinear polarization [22]; or (iii) the linearly polarized rf field is applied in the presence of a static field that has a different polarization [24]. In all of these scenarios (an incomplete list of possibilities), the cylindrical symmetry of the electron binding potential is destroyed, and m is no longer a good quantum number. Fortunately, a straightforward extension of the preceding analysis of ℓ mixing in a static electric field can be used to understand the change in AI, PD, and DR rates when both ℓ and m are mixed. If m remains a good quantum number, the field redistributes the character of a few low-ℓ states over approximately n levels with the same low value of m. If m is not a good quantum number, the field smears the low-ℓ character over $\sim n^2$ states for each principal quantum number n. Assuming perfectly uniform mixing, this leads to the creation of AI and PD rates, Γ'_{AI_S} and Γ'_{PD_S} that are identical for all states in a given n manifold. Γ'_{AI_S} and Γ'_{PD_S} are reduced in magnitude relative to the respective rates of the pure low-ℓ states by factors of order of $1/n^2$. If n is not too large, Γ'_{AI_S} will usually still be greater than γ. Accordingly, the contribution of each n state to the total DR rate is enhanced by $\sim n^2$ relative to the zero-field case due to the increase in the number states, whose AI rate exceeds the spontaneous emission rate γ.

There are a number of practical motivations for studying AI, PD, and/or DR in the presence of fields. For example, DR in plasmas takes place in the presence of microfields which have nearly static as well as fast transient components, due to nearby ions and electrons, respectively [12,26]. In laboratory plasmas, electric and magnetic containment fields are also often present. Therefore, our ability to accurately predict dynamics in astrophysical and fusion plasmas depends critically on our understanding of DR rates in the presence of such fields. As another example, consider zero electron-kinetic energy (ZEKE) spectroscopy, a useful technique for measuring vibrational and rotational spectra of molecular ions. ZEKE spectroscopy is based on the detection of very long-lived, highly excited Rydberg states associated with different ionic core states of the molecule [27]. It has been established that weak static fields and the presence of background ions enhance the ZEKE signal (i.e., the number of long-lived Rydberg states) presumably due to the suppression of AI and PD through angular momentum mixing in the field [28–35].

Several recent experiments have utilized rf and microwave radiation with linear, elliptical, and circular polarization to simulate the transient fields experienced by neutral and charged species in a plasma [13,24,25]. However, there are important differences in the physics that determines the rates for AI, PD, and DR in systems that are exposed to long oscillatory field pulses as opposed to the rapid collisional transients that are actually present in plasmas. An oscillatory pulse continuously drives transitions between different Rydberg states so that, on time average, the levels are angularly mixed. On the other hand, a single transient field pulse transfers population from some initial level (or levels) and produces a linear superposition of different *pure* angular-momentum states [36]. The angular momentum of the superposition state is not continuously mixed in the absence of the field. The evolution of this coherent wave packet can be very different from that of a mixed angular-momentum state. For example, if a transient field creates a linear superposition of high- and low-ℓ states, only the low-$\ell < \ell_c$ part of the wave function will participate in AI or PD. The remaining high-ℓ components eventually stabilize, via spontaneous emission or another relaxation process. Therefore, while a static or oscillatory field can alter AI and PD rates through angular-momentum mixing, transient fields might elliminate these decay channels by angular-momentum *transfer*. If Rydberg atoms and molecules can indeed stabilized by the application of an appropriate electric-field pulse, then very short electric transients may find application in time domain pump-probe spectroscopy of quantum dynamics in doubly excited systems [37–39].

In the subsequent sections we describe the results of experimental and theoretical investigations of the effects of transient electric fields on autoionizing Rydberg states in calcium. We focus on the impulsive regime where the duration of the field pulse is less than the classical Kepler period of

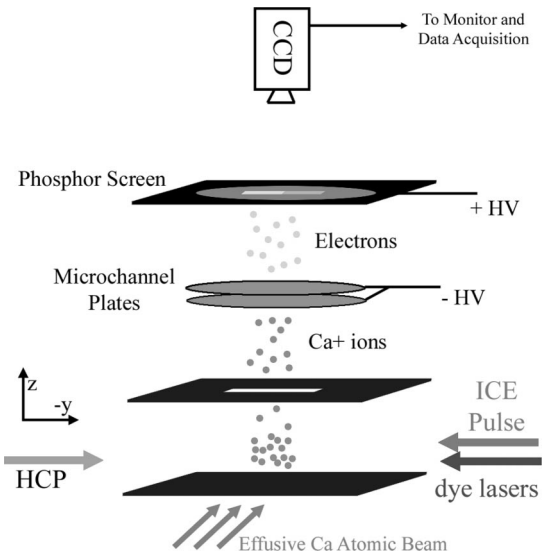

FIG. 1. A schematic diagram of the laser-atom interaction region and detection apparatus. The counterpropagating HCP and ICE laser allow for a range of time delay information to be recovered in a single laser shot [41].

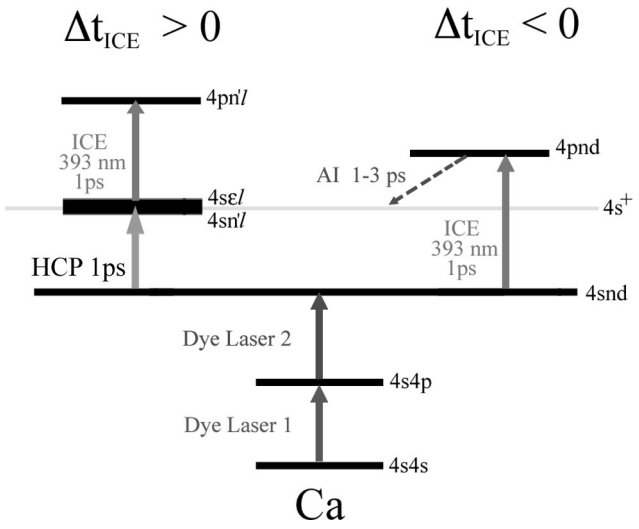

FIG. 2. Laser excitation schematic for the experiment.

the Rydberg electron. To the best of our knowledge, until this work, the effects of impulsive fields on autoionizing atoms was experimentally unexplored. We explicitly consider several different field configurations, including: (i) a linearly polarized transient field in the presence of a static field with the same polarization direction; (ii) two time-delayed transient field pulses with orthogonal linear polarizations; and (iii) a linearly polarized transient field in the presence of a static field with an orthogonal polarization. We find no evidence for stabilization against AI using field configuration (i), but up to 10% of the atoms exposed to fields of type (ii) and (iii) are stabilized. Our experimental results can be qualitatively explained using semiclassical arguments and are well reproduced by numerical quantum simulations.

II. EXPERIMENTAL METHOD

The basic procedure for all three experiments is as follows. Two dye lasers excite Ca atoms from the $4s\,4s$ ground state into a $4snd$ Rydberg level. A short ($\sim$1 psec) laser pulse then drives an isolated core excitation (ICE) of the $4snd$ atoms, producing a doubly excited $4pnd$ autoionizing state [40]. The Rydberg atoms are exposed to a 1-psec electric-field pulse at some time Δt_{ICE} relative to the ICE. The total ion yield resulting from either AI or transient field ionization is measured as a function of the pulsed field strength, the frequency of the laser driving the ICE transition, and the time delay Δt_{ICE} between the ICE and transient field pulses.

The experiment takes place in a vacuum chamber with a base pressure of 10^{-6} torr. Figure 1 shows a schematic of the interaction region and detector assembly. A diagram of the laser excitation scheme is presented in Fig. 2. The interaction region is defined above and below by a pair of 100 cm^2 parallel capacitive field plates spaced by 1.5 cm. A resistively heated oven produces a thermal beam of Ca atoms ($\rho \sim 10^8$ atoms/cm^3) that enters the interaction region along the $\hat{x}$ direction. A 432 nm 5-nsec dye laser pulse passes through the interaction region along the $\hat{y}$ direction. This pulse promotes Ca atoms from the $4s\,4s$ ground state to an intermediate $4s\,4p$ level. A second 5-nsec laser pulse is created by mixing the $\sim$620 nm output from a dye laser with the 1064 nm fundamental output from a Nd:YAG (YAG denotes yttrium aluminum garnet) laser in a potassium dihydrogen phosphate (KDP) crystal. This pulse also enters the interaction region along $\hat{y}$ and excites atoms in the intermediate $4s\,4p$ level to some $4snd$ Ca Rydberg eigenstate. The spectral bandwidth of the second pulse is approximately 0.5 cm^{-1} and its central wavelength is tunable from 389 nm–393 nm, allowing the excitation of a range of $4snd$ levels with $15<n<70$. A third laser pulse, with a duration of 1 psec and a central wavelength of 393 nm enters the interaction region parallel to the nanosecond laser beams. The 1 psec pulse has a spectral bandwidth of $\approx$20 cm^{-1} and is created by frequency doubling the 120 fsec, 786 nm output of a Ti:sapphire laser in a 3-cm long KDP crystal [42]. The 1 psec pulse resonantly drives the ionic $4s^+$-$4p^+$ transition in the $4snd$ Rydberg atoms, producing autoionizing $4pnd$ states. The Rydberg electron is essentially a spectator during this ''isolated-core'' excitation (ICE) [40]. Unless they are perturbed by an additional external field, the $4pnd$ atoms autoionize over a time interval roughly equal to τ_K for that particular Rydberg state [37–39]. All of the lasers are linearly polarized along the vertical $\hat{z}$ axis, and the intermediate and final Rydberg states have zero projection of total angular momentum on this axis, $M=0$. For simplicity, the 1 psec pulse that facilitates the ICE transition will be referred to as the ICE laser or ICE pulse for the remainder of the paper.

At some time delay Δt_{ICE} preceding or following the ICE pulse, the Rydberg atoms are exposed to one or more transient field pulses. The transient field is generated by illuminating a biased GaAs photoconductive switch with the 786 nm output of the Ti:sapphire laser [43]. The radiation pulse that propagates through the GaAs switch has a nearly unipo-

lar time-dependent electric field and is commonly called a half cycle pulse (HCP) [44]. The HCP field has a full width at half-maximum duration of ~ 1 psec and is linearly polarized along the bias field direction. Small nonunipolar features in the HCP are reduced in amplitude through the use of a second, unbiased GaAs wafer that acts as a transient attenuator [45]. The GaAs switch is located in the vacuum chamber and, using a parabolic mirror, the HCP is directed into the interaction region antiparallel to the three laser beams. The HCP redistributes population from the initial nd Rydberg state into a coherent superposition of $n'\ell'm'$ states [36]. The details of the final-state distribution depend on the principal quantum number of the initial Rydberg state, the strength and orientation of the HCP, and on the strength and orientation of any static electric fields that are present. However, previous measurements have shown that relatively weak HCPs, with peak amplitudes <1 kV/cm can transfer significant population to high-ℓ levels [36].

Approximately 500 nsec following the ICE and HCPs, a ~ 75-V clearing pulse is applied to the lower-field plate. Ions present in the interaction region, formed through AI or HCP ionization, are accelerated towards a slit in the upper-field plate. The clearing field, ~ 50 V/cm, has sufficient strength to ionize Rydberg atoms with $n>50$. Therefore, any neutral Rydberg atoms with $n>50$ present in the interaction region are indistinguishable from ions. Ions passing through the slit in the upper-field plate strike a pair of microchannel plates backed by a phosphor screen. Electrons generated by ion impact on the microchannel plates strike the phosphor screen, causing it to fluoresce. The fluorescence is detected with a charge coupled device (CCD) camera and the video output from the CCD camera is fed to a computer. Since the HCP and the ICE pulse counterpropagate through the interaction region, atoms at different locations beneath the extraction slit experience a different time delay Δt_{ICE}, between the HCP and the ICE. Therefore, delay information is encoded into the spatial position of the ions that strike the microchannel plates, and the fluorescence from the phosphor screen provides an image of ionization yield vs Δt_{ICE} for a particular HCP field strength and ICE laser wavelength [41]. Approximately 100 psec of delay information is obtained in each laser shot with 1 psec resolution [41]. The apparatus runs at a 15-Hz repetition rate.

While our primary interest is in HCP induced stabilization of autoionizing atoms, it is important to keep in mind that an HCP of sufficient strength is capable of ionizing Rydberg atoms directly [44]. An atom that is stabilized by angular-momentum transfer but then ionized by the pulse still results in the production of an ion and a free electron. The only observable difference between the two processes is the final electronic state of the ion and the energy and angular momentum of the ejected electron. Since we measure total ion production only, we cannot distinguish between the two possible ionization mechanisms.

As noted in the introduction, measurements have been performed for three different electric-field configurations. First, we consider the effect of exposing the autoionizing atoms to a single, linearly ($\hat{z}$) polarized HCP. In this scenario, the z projection of Rydberg angular momentum, m, remains a good quantum number during the interaction with the HCP field. Second, we use a combination of two temporally identical, but orthogonally polarized HCPs as the transient field. The two HCPs are separated in time by a delay Δt_{HCP}. When Δt_{HCP} is comparable to the duration of a single HCP, the net field closely resembles that experienced by a Rydberg electron during a collision with a charged particle [46]. In this case, $\Delta m \neq 0$ transitions are allowed, and following the HCP, the Rydberg electron is left in a superposition of different m states. Third, we examine the effect of exposing the atoms to a linearly polarized HCP in the presence of an orthogonally polarized static electric field. $\Delta m \neq 0$ transitions are allowed in this configuration as well.

III. RESULTS

For the three field configurations, the ion yield vs Δt_{ICE} data are essentially bilevel curves for all values of HCP field strength (F_{HCP}) and ICE laser frequency. Within our signal to noise, the ion yield vs Δt_{ICE} has constant values for negative and positive Δt_{ICE}, respectively. The delay independence of the ion signal is expected at negative delays of more than a few picoseconds. In this case, all of the atoms excited to $4pnd$ states have autoionized before the arrival of the HCP, so the HCP has no effect on the ion yield or AI rate. For $\Delta t_{ICE}>0$, the HCP arrives before the ICE, interacts with singly excited $4snd$ atoms. Depending on the field configuration and strength, the HCP(s) produces atoms in a coherent superposition of different $4sn'\ell'$ states. Following the HCP, this Rydberg wave packet evolves for a time Δt_{ICE} before the ICE [36]. Our measurement, of a delay independent ion yield that is distinctly different for negative and positive ICE delays, indicates that the creation of a coherent superposition state by the HCP does indeed affect the AI rate and/or ion yield. However, it also shows quite clearly that the ICE probability and AI rate are not strongly affected by the temporal evolution of the wave packet. This is quite interesting considering that investigations of time-resolved ICE of radially localized $4snd$ wave packets show a significant variation in ICE cross section as the wave packet moves radially between its inner and outer turning points [42,47]. Apparently the wave packet produced by the HCP lacks a coherent radial breathing motion that is crucial for affecting the ICE probability. This supposition is supported by previous measurements of the evolution of a Rydberg electron following its exposure to an HCP [48]. It is also worth noting that a significant decrease in the AI signal is observed, whenever the HCP and ICE pulses overlap in time and the HCP is too weak to directly ionize the atom. This effect, which is not completely understood at this time, provides a convenient marker for determining $\Delta t_{ICE}=0$.

A. Single HCP measurements

In the first experiment, ion yield is measured as a function of ICE laser frequency and Δt_{ICE} for several fixed values of F_{HCP}. In Fig. 3(a) we show representative curves for $\Delta t_{ICE}>0$ and $\Delta t_{ICE}<0$ for an initial $4s\,19d$ eigenstate exposed to a HCP with $F_{HCP}\approx 3$ kV/cm. This HCP field

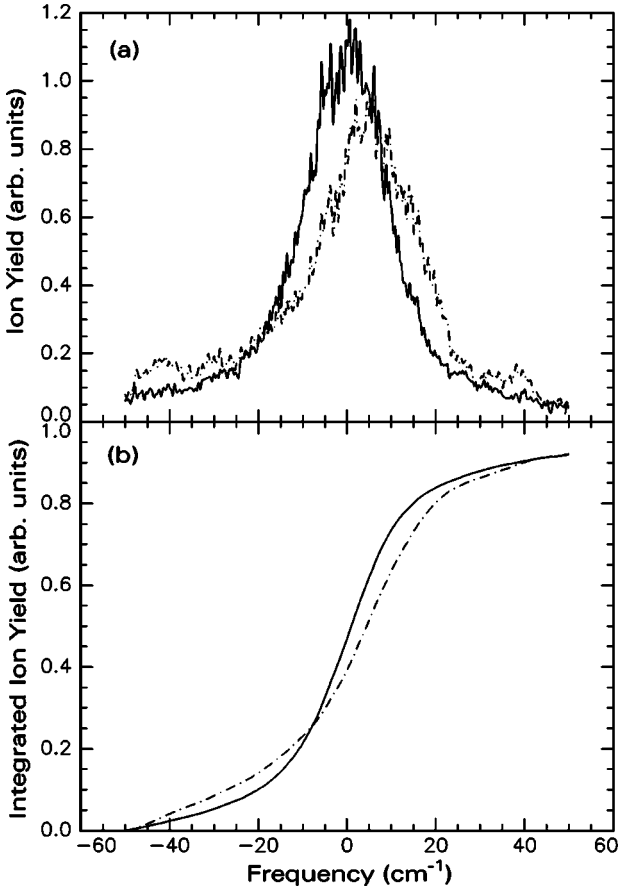

FIG. 3. (a) Observed ion yield plotted as a function of the detuning of the ICE laser from the $4s^+ \rightarrow 4p^+$ transition. The solid curve represents the in-field case ($\Delta t_{ICE} > 0$), while the dashed curve corresponds to the zero-field case ($\Delta t_{ICE} < 0$). The initial state is $4s\ 19d$ and the maximum HCP field is 2.5 kV/cm. (b) Integrated ion yield as a function of frequency. Note that the integrated ion yield is the same for $\Delta t_{ICE} > 0$ and $\Delta t_{ICE} < 0$.

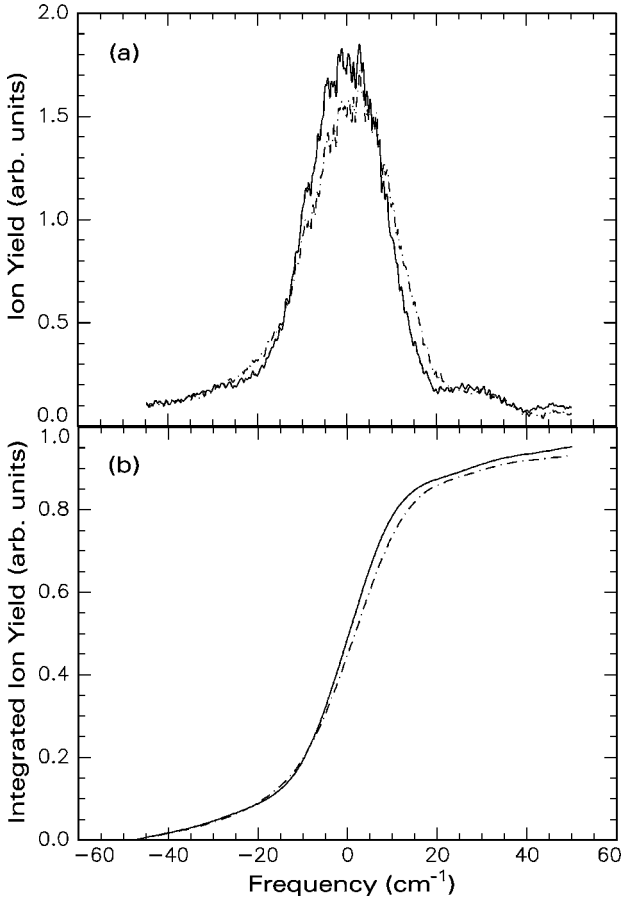

FIG. 4. (a) Observed ion yields as a function of the detuning of the ICE laser from the $4s^+ \rightarrow 4p^+$ transition for an initial $4s\ 27d$ state. The solid curve represents the in-field case ($\Delta t_{ICE} > 0$), while the dashed curve corresponds to the zero-field case ($\Delta t_{ICE} < 0$). The maximum HCP field is 2.5 kV/cm. Integrated ion yield is shown in (b). As in Figure 3, no suppression of AI is observed.

strength results in the greatest difference between the $\Delta t_{ICE} < 0$ and $\Delta t_{ICE} > 0$ curves. As explained above, the $\Delta t_{ICE} < 0$ data provides a measure of the ion yield in the absence of the HCP. Therefore, for simplicity, we will refer to the $\Delta t_{ICE} > 0$ and $\Delta t_{ICE} < 0$ data as "in field" or "zero field," respectively.

Inspection of the two curves in Fig. 3(a) shows that for some ICE laser frequencies, fewer ions are produced for the in-field case as compared to the zero-field case. This is the expected result if the action of the HCP has indeed stabilized the atoms against AI. However, at other frequencies the data shows the opposite effect. In fact, it is the line shape of the ICE resonance that has been modified by the HCP, not the branching ratio for decay via autoionization rather than spontaneous emission. The center of the zero-field AI resonance is noticeably shifted relative to the in-field case. In zero field, the difference between the quantum defects of the $4s\ 19d$ and $4p\ 19d$ states results in a resonance frequency which is detuned from the $4s^+$-$4p^+$ ionic transition. However, the HCP populates high-ℓ states that have negligble quantum defects in both the $4s$ and $4p$ core configurations. As a result, the in-field resonance appears at the ionic transition frequency [40]. Note that the extremely low AI rate out of the high-ℓ states should also result in extremely narrow in-field ICE resonances. However, the linewidth is instrument limited to $\approx 20\ \text{cm}^{-1}$ due to the bandwidth of the 1-psec ICE laser pulse. From the measured line-shapes analysis, it appears that the action of the HCP results in the population of higher-ℓ states. But does any stabilization occur?

To answer this question, we take advantage of the fact that the area under the ICE resonance must be independent of the initial Rydberg state and, therefore, must be identical for the in-field and zero-field measurements. Since (in the absence of HCP ionization) the number of singly excited Rydberg atoms is the same before and after the HCP, any difference in the frequency integrated ion yield for the two cases indicates a difference in the AI probability following the ICE. The in-field and zero-field ion yields integrated over ICE excitation frequency are shown in Fig. 3(b). The integrated yields are identical within the experimental error, indicating no HCP induced stabilization against autoionization.

In Fig. 4 the in-field and zero-field ionization signal is shown for a $4s\ 27d$ initial state and $F_{HCP} = 2.5$ kV/cm. Because the difference in the quantum defects between the

$4s\,27d$ and $4p\,27d$ states is less than that for the $4s\,19d$ and $4p\,19d$ levels, the shift in the AI resonance is less than in Fig. 3(a). Also, due to their reduced AI and resonance widths, the true $4p\,27\ell$ resonance line shapes are more severely masked by the 20-cm^{-1} ICE laser bandwidth. Once again, however, the integrated ion yields are nearly identical. Similar results are obtained for all initial Rydberg states studied.

The apparent absence of HCP induced AI stabilization is rooted in two different physical phenomena. The first is HCP ionization. A single impulsive HCP puts both energy and angular momentum into the Rydberg electron [36,44]. An HCP, which has sufficient strength to transfer a substantial fraction of the Rydberg population to states with $\ell > \ell_c$ (≈ 7 for the $4pn\ell$ levels in Ca) also increases the energy of the electron to the point where it is ionized (or has principal quantum number $n > 50$ and is counted as ionized due to the fields in our spectrometer). The second effect is an experimental artifact that has significant practical relevance. The HCP has a low amplitude ''tail'' of opposite polarity that follows the primary pulse. This tail can extend for hundreds of picoseconds or even nanoseconds with an amplitude of a few V/cm [45]. Therefore, following the HCP, the Rydberg atoms evolve in a small nearly static field that is similar to the microfields produced by ions in a plasma. Consequently, even though the HCP induces angular-momentum *transfer* that should stabilize some fraction of the atoms from AI, the static field *mixes* low-ℓ character back into the Rydberg wave function. As a result, the mixed state has an AI rate that exceeds the spontaneous emission rate, and the atoms autoionize with 100% efficiency. These statements are supported by the results of the quantum numerical simulations described in the discussion section.

B. Measurements with two orthogonal HCPs

Next we investigate AI stabilization induced by two temporally identical, time-delayed, and orthogonally polarized HCPs. In particular, we consider relative HCP time delays, Δt_{HCP} that are comparable to the 1 psec duration of the two equal amplitude HCPs. This combination of HCPs has physical relevance since the time-dependent field closely resembles that experienced by an atom undergoing a long-range collision with a charged particle [46]. Due to the time-dependent polarization of the combined HCP field, m is not conserved during the HCP-atom interaction. Therefore, depending upon the combined field amplitude, the pulse produces a Rydberg wave packet that is a coherent superposition of different n,ℓ,m states.

The two HCPs are generated using different GaAs switches. Each pulse enters the interaction region at a small angle relative to the $\hat{x}$ axis and approximately perpendicular to the ICE pulse (see Fig. 5). In this geometry, ion yield is measured as a continuous function of Δt_{HCP} in a single laser shot [41]. The ICE pulse propagates along the $+\hat{y}$ direction, colinear with the slit in the upper-field plate, and at some delay Δt_{ICE} relative to the HCP sequence. The near 90° crossing angle between the HCP and ICE beams means that collected ions have Δt_{ICE} values that vary by a few picoseconds across the narrow dimension of the slit. This uncertainty can be reduced to less than the 1 psec time resolution of the ICE and HCPs by including in our analysis only those ions at the center of the slit image. Alternatively, errors due to the uncertainty in Δt_{ICE} can be eliminated by choosing HCP delays of >10 psec and <-10 psec for the in-field and zero-field cases, respectively. This method works because, as stated previously, the ion signal is constant for $\Delta t_{ICE} > 0$ (the in-field case) and for $\Delta t_{ICE} < 0$ (the zero-field case).

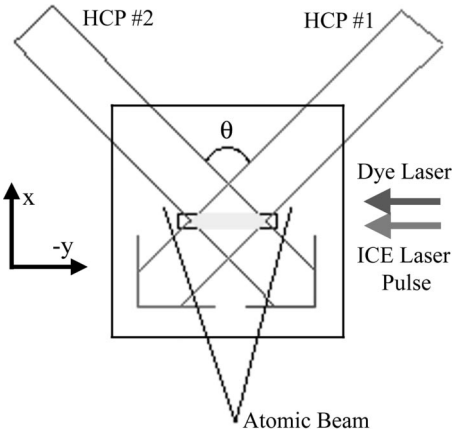

FIG. 5. A schematic diagram of the experimental approach used to measure AI suppression due to two orthogonal HCP fields. HCP1 is polarized along $+\hat{z}$ and moves through the interaction region at some small angle $\theta/2$ to the $-\hat{x}$ direction. HCP2 is approximately polarized along $+\hat{y}$ and moves through the interaction region at an angle $-\theta/2$ to $-\hat{x}$. A spatially dependent time delay Δt_{HCP} exists between the two HCP fields. The point in the interaction region where the two pulses arrive simultaneously ($\Delta t_{HCP}=0$) is defined to be $y=0$. Typically $\theta < 10°$, and we can study a range of -20 psec$< \Delta t_{HCP} <$ 20 psec.

In Fig. 6, we show in-field and zero-field curves that are completely analogous to those shown in Figs. 3 and 4. The data in Fig. 6 are obtained with an initial $4s\,20d$ Rydberg level and $F_{HCP} \approx 3$ kV/cm for each of the two orthogonal pulses. As with a single HCP, population transfer to high angular-momentum states results in an in-field AI line shape that is narrower and shifted toward the ionic transition. However, a slight suppression ($\approx 10\%$) of the frequency integrated ion yield is observed when $\Delta t_{ICE} > 0$. Measurements performed with other initial n states show similar stabilization percentages.

We also examine the effect of varying the relative time delay between the two HCP fields on the ion yield. Figure 7 shows the frequency integrated ion signal as a function of the delay Δt_{HCP} between the two HCPs. For this data scan, the ICE pulse delay is set so that $\Delta t_{ICE}=0$ when $\Delta t_{HCP}=0$ at the center of the extraction slit. Therefore, the zero-field data appears at negative values of Δt_{HCP} and the in-field measurement is shown at positive Δt_{HCP}. Of course, from symmetry, the in-field signal is symmetric about $\Delta t_{HCP}=0$. This symmetry is not obvious in Fig. 7 due to the positioning of $\Delta t_{ICE}=0$ at $\Delta t_{HCP}=0$. The data is displayed in this way to highlight the small, but significant, AI stabilization that is

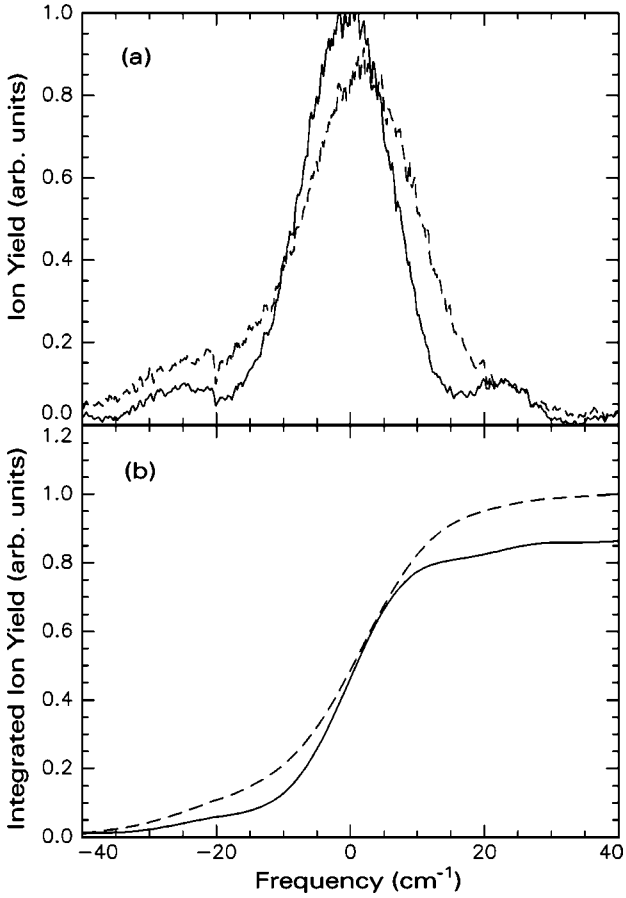

FIG. 6. (a) Observed ion yield as a function of the detuning of the ICE laser from the $4s^+ \rightarrow 4p^+$ transition. The solid curve is the in-field case ($\Delta t_{ICE} > 0$), and the dashed curve is the zero-field case ($\Delta t_{ICE} < 0$). The initial eigenstate is $4s\ 20d$ and each HCP field has a maximum field of ≈ 3 kV/cm with $\Delta t_{HCP} \approx 5$ psec. Integrated ion yield is plotted in (b) analgous to Figs. 3,4. A small amount of AI suppression ($\approx 10\%$) is observed.

induced by the HCP fields. Our measurements indicate that the stabilization effect is relatively insensitive to the delay between the two HCPs. Clearly, the stabilization observed with the two HCPs is facilitated by population transfer to levels with high m and high ℓ. This is in contrast to the single HCP measurements where states with low m and high ℓ are populated and no stabilization is observed.

C. Measurements with orthogonal HCP and static electric fields

Finally, we investigate the stabilization of AI due to the combined action of orthogonally polarized HCP and static electric fields. A constant voltage applied to the upper-field plate produces a uniform static field F_S along the $\hat{z}$ direction in the interaction region. The magnitude of the field is less than the Inglis-Teller field, $F_S = 1/3n^5$ where states from adjacent n manifolds cross [5]. In the presence of the field, the second dye laser excites an incoherent mixture of several $m=0$ Stark eigenstates within the 0.5 cm^{-1} laser bandwidth. The frequency of the second laser is tuned to either the location of the d state in zero field or the manifold state with the most extreme negative Stark shift. After the dye laser excitation, a single HCP (linearly polarized along $\hat{x}$) enters the interaction region. Because the static field defines the quantization axis for the atoms, m is not a good quantum number in the presence of the HCP, and population may be transferred to higher-m Stark states. Recall that even though the high-m Stark states are angularly mixed, they contain no low-ℓ character. Therefore, for $m \gtrsim \ell_c$ these states should be stable against AI.

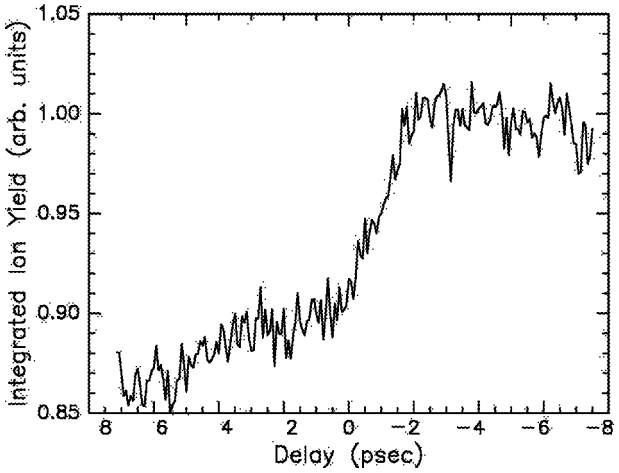

FIG. 7. Frequency integrated ion yield as a function of relative HCP delay, Δt_{HCP}. $\Delta t_{ICE} = 0$ is at the same point as $\Delta t_{HCP} = 0$. Therefore, negative values of Δt_{HCP} correspond to the zero-field case, as described in the text.

As in the other two field configurations, ion yield is measured as a function of ICE laser frequency for a number of different static field and HCP field values. Typical experimental results for the in-(HCP) field and zero-(HCP) field integrated ion yields are shown in Fig. 8. The data in Fig. 8 are obtained for an initial $n=22$ manifold state with $F_S = 50$ V/cm and $F_{HCP} \approx 3$ kV/cm. As in the case of two orthogonally polarized HCPs, the in-(HCP)field AI probability is suppressed by $\sim 10\%$ relative to the zero-(HCP) field case. The dynamical evolution of the Rydberg electron during and s ubsequent to its interaction with the orthogonal fields is very different for the two configurations, [HCP$\times$HCP] or [HCP$\times$static field]. Nevertheless, similar stabilization probabilities are observed for the two cases. Clearly, the key to AI suppression is a population transfer to high-m states.

IV. DISCUSSION AND NUMERICAL ANALYSIS

As discussed previously, doubly excited $4pn\ell$ states will autoionize for $\ell \lesssim \ell_c$ and will be stabilized by spontaneous emission of the $4p$ core electron for $\ell > \ell_c$. Here, ℓ_c defines the state for which the $4pn\ell$ autoionization lifetime equals the 3-nsec spontaneous emission lifetime of the $4p$ state of Ca^+ [49]. The first step in obtaining a quantitative understanding of the experimental results is a determination of ℓ_c for the $4pn\ell$ system. We begin by computing the autoionization rates for the $4pn\ell$ states from Fermi's Golden rule in the isolated resonance approximation [10]. We ignore spin

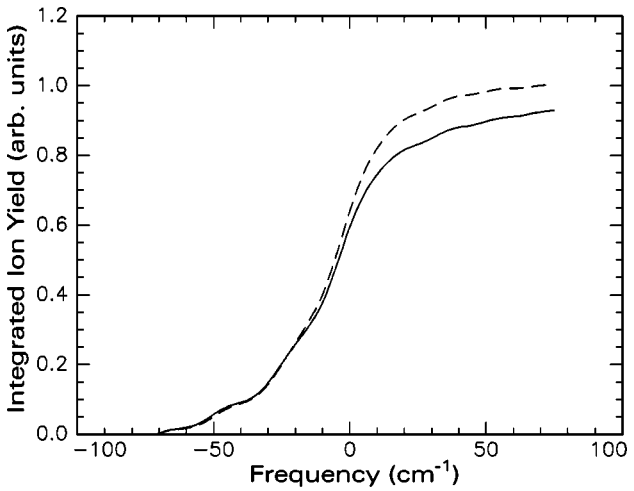

FIG. 8. Integrated ion yield as a function of detuning from the ionic $4s^+ \rightarrow 4p^+$ transition. The initial state is a mixture of $4s\,22k$ Stark states in a 50 V/cm static field. The solid curve shows the in-field case ($\Delta t_{ICE} > 0$) and the dashed curve is the zero-field case. The same static field is present in both cases. The HCP has a peak field of ~ 3 kV/cm and is polarized orthogonal to the static field. As in the case of two orthogonally polarized HCPs, a small amount of AI suppression is observed.

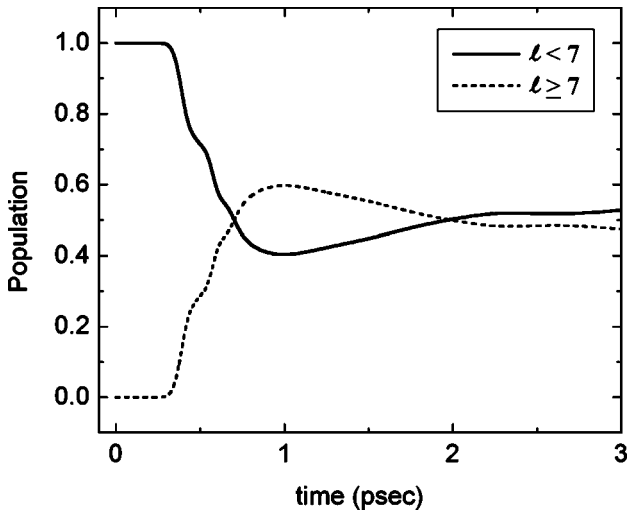

FIG. 9. Result of the quantum-mechanical simulation of the interaction of a single HCP field with an autoionizing state as discussed in the text. The initial Rydberg state has $n=22$, $\ell=2$, and $m=0$, and the HCP has a peak field of 5 kV/cm with a static negative tail of 10 V/cm. The solid curve shows the population in low-ℓ states ($\ell<7$), while the dashed curve shows the population in high ℓ.

and assume that the bound $4pn\ell$ autoionizing state is coupled to the $4s\epsilon,\ell\pm1$ and $3d\epsilon,\ell\pm1$ continua by the dipole term in the expansion of the electron-electron Coulomb interaction. The radial matrix elements are computed using numerical Numerov integration and hydrogenic radial wave functions are used for the continua [50]. The total AI rate is taken as the sum of the rates into the $4s$ and $3d$ continua. For the range of n states studied, we find that $\ell_c \approx 7$.

In an attempt to quantitatively reproduce the experimental results and confirm our qualitative explanation of those results, we have numerically integrated the time-dependent Schrodinger equation for a calcium Rydberg atom under the influence of an electric field in each of the three experimental configurations. We utilize a fourth-order Runga-Kutta integration routine and use angular-momentum eigenstates as basis functions. The calculation is performed in the ''length gauge'' under the dipole approximation, ignoring spin. Radial matrix elements are computed using Numerov integration [50] of Coulomb wave functions using the known quantum defects of Ca $4sn\ell$ Rydberg states.

In the simulation of the first experiment, the single linearly polarized HCP is modeled as a Gaussian field with a duration of 1 psec, full width at half maximum. The effect of the negative tail of the HCP is included by adding, for all times following the peak of the HCP, a constant negative component of 10 V/cm to the total field. All n and ℓ states for $10<n<90$ are included in the calculation. However, because m remains a good quantum number in the field, only $m=0$ levels are considered. Just prior to the rise of the Gaussian HCP field ($t=0$), the population in the initial Rydberg state is set to 1. The system is allowed to evolve for the lifetime of the $4p^+$ core electron under the influence of the main HCP and its negative tail. The effect of AI is simulated by removing probability amplitude from each angular-momentum state according to its calculated autoionization rate. We assume that autoionization commences immediately following the HCP. HCP ionization is included by absorbing any probability amplitude reaching the highest n state ($n=90$). This boundary is well into the effective continuum of the experiment since states with $n>50$ are ionized in our spectrometer.

Figure 9 shows the time-dependent high- and low- ℓ populations, during the HCP, for an initial $4s\,22d$ state exposed to a peak HCP field of $F_{HCP}=5$ kV/cm. While higher fields result in greater fractional population of high-ℓ states, they also produce significant HCP ionization. The results in Fig. 9 represent nearly the best case; over 50% of the initial population is located in high-$\ell > \ell_c$ states when AI commences. However, as shown in Fig. 10, at the end of the simulation less than 1% of the initial population remains unionized.

The ''stair-step'' decrease in Rydberg population that is shown in Fig. 10 is due to the coherent evolution of angular momentum in the tail of the HCP field. Immediately after autoionization commences, the fraction of the Rydberg population that has low-ℓ character rapidly ionizes. At this time, all of the surviving bound population resides in high-ℓ states. However, the small static field causes a precession of the angular momentum in the ''Stark wave packet'' from high into low ℓ [51–53]. After one ''Stark period,'' $\tau_S = 2\pi/(3F_{tail}n)$, a significant fraction of the bound population again has low-ℓ character [51–53]. Autoionization of the low-ℓ part of the wave packet results in another rapid decrease in the Rydberg population. The cycle repeats until the atom has completely ionized. In the best case (i.e. the greatest survival probability), the simulation predicts less than 10% surviving Rydberg population after 1 nsec and less than 1% remaining after the 3-nsec $4p$ core lifetime. The

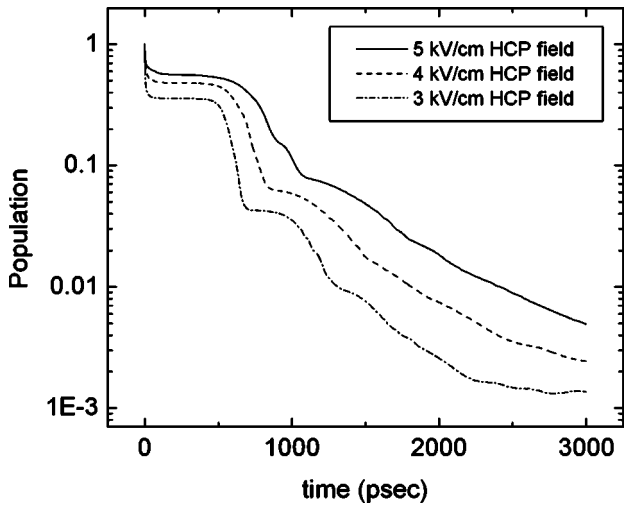

FIG. 10. Surviving Rydberg population as a function of time calculated under the same conditions as in Fig. 9. The system is allowed to autoionize after a time $\Delta t_{ICE}=1.5$ psec according to the calculated AI rates for calcium. The calculated surviving population is shown as a function of time for three values of HCP field strength. Less than 1% of the initial population remains after 3 nsec.

effective autoionization rate is proportional to the magnitude of the static field. Choosing a HCP tail field of 20 V/cm would result in an autoionization lifetime that is half of that indicated in Fig. 10. Clearly, angular momentum mixing in the small HCP tail effectively erases the stability of the high-ℓ states that are populated during the impulsive component of the HCP. The results of the calculation are in good agreement with the experimental observation that the action of the single HCP causes no reduction in the ionization yield.

From the single pulse simulation it is apparent that Stark mixing due to the HCP tail, or any other static field that is present, will prevent AI stabilization for Rydberg population that has $m<\ell_c$. Here m is the projection of Rydberg angular momentum *along the static field axis*, $\hat{z}'$, not necessarilly along the lab-fixed z axis. However, since m is a good quantum number in the presence of the static field, any final-state amplitude with $m>\ell_c$ will be stabilized. Therefore, for the crossed field configurations [HCP $\times$ HCP] or [HCP $\times$ static field], the fraction of the autoionizing atoms that are stabilized by the field is equal to the high-m ($>\ell_c$) population probability following the HCP(s). Of course, for crossed fields all m states for each value of ℓ must be included in the calculation. As a result, memory limitations restrict the principal quantum number range of the basis states to $10<n<45$. In all other respects, the calculation is the same as for the single HCP case.

For two crossed polarized HCPs, the static field produced by the sum of the pulse tails defines the proper axis $\hat{z}'$ along which m must be evaluated. This axis lies at an angle of 45° relative to the polarization direction of the main HCPs. Figure 11 shows the calculated final-state m distribution following the passage of two orthogonally polarized HCPs. The pulses have a relative delay of 0.8 psec, but calculations performed with other delays showed similar results. The initial state for the simulation is $4s\,22d$ with $m=0$ along the lab-fixed z axis, and the amplitude of each pulse is $F_{HCP}=3$ kV/cm. The HCP fields are polarized along $\hat{x}$ and $\hat{z}$, respectively, so in the presence of the pulse tails, the appro-

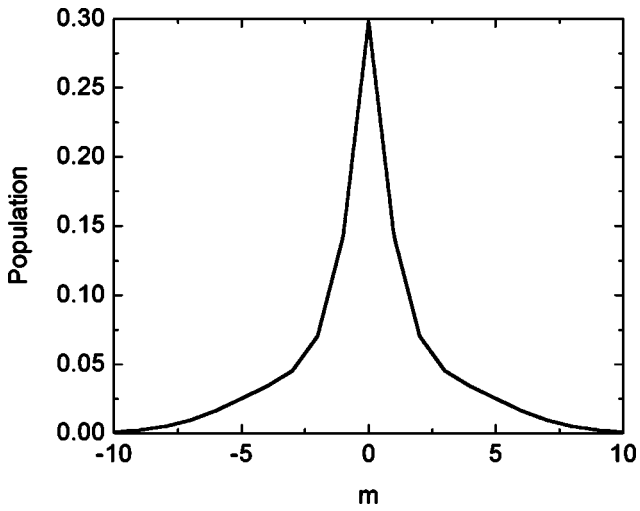

FIG. 11. Result of the quantum-mechanical simulation of the interaction of two orthogonal HCP fields with an autoionizing state as discussed in the text. The initial Rydberg state has $n=22$, $\ell=2$, and $m=0$, and each HCP has a peak field of 3 kV/cm with a static negative tail of 10 V/cm. The first HCP is polarized along $\hat{z}$, and the second HCP is polarized along $\hat{x}$. The time delay between the two pulses is $\Delta t_{HCP}=0.81$ psec. The m distribution is shown 2 psec after the HCP interaction as measured along the $(1/\sqrt{2})(\hat{x}+\hat{z})$ axis. Approximately 8% of the population has $m>\ell_c$.

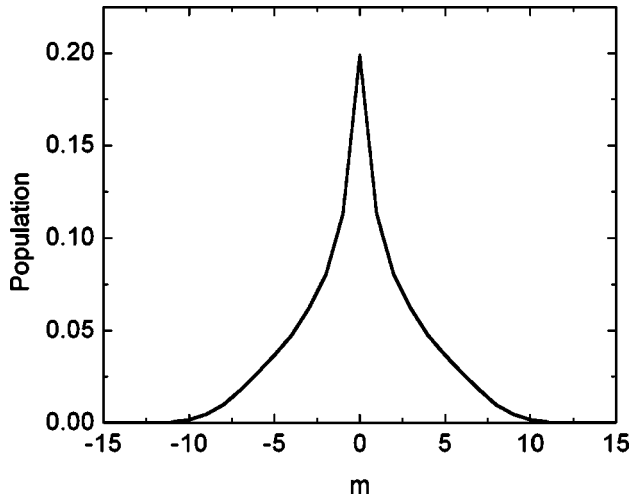

FIG. 12. Results of the quantum-mechanical simulation of the interaction of an HCP field with an orthogonally applied static field as discussed in the text. Initially, an ensemble of $4s\,22k$ states is excited in a 200 V/cm static field. The initial-state energy distribution is centered around the zero-field location of the $4s\,22d$ state. The static field is oriented along the $\hat{z}$ axis. The HCP is polarized in the $\hat{x}$ direction and has a peak field of 3 kV/cm with a 10 kV/cm static field tail. The m distribution as measured along the $\hat{z}$ axis is shown 2 psec after the HCP interaction. Less than 10% of the population has $m>\ell_c$ after the HCP interaction.

priate quantization axis is $\hat{z}' = (1/\sqrt{2})(\hat{x}+\hat{z})$ after the passage of the two pulse sequence. Approximately 10% of the final Rydberg population resides in states with $m > \ell_c$, and therefore, are stable against autoionization. This value is in good agreement with our experimental observation of $\approx 10\%$ stablilization probability for two crossed polarized HCPs.

We have also performed calculations for crossed HCP and static fields. In this case, the only additional complication relative to the simulation using two crossed HCPs is the specification of the initial state. We assume the dye laser excites a superposition of Stark states within the laser bandwidth at some mean energy within a given Stark manifold. The excitation cross section and ℓ-state composition of the initial state is computed by diagonalizing the Hamiltonian for our limited calcium basis in the presence of a static field. Figure 12 shows the final-state m distribution assuming that the mean excitation energy of the initial Stark state superposition is equal to that of the $4s\,22d$ level in zero field. In the simulation, the 200 V/cm static field points in the $\hat{z}$ direction while the 3 kV/cm HCP is polarized along $\hat{x}$. Due to the relatively small amplitude of the HCP tail, the final quantization axis $\hat{z}' \approx \hat{z}$. Following the HCP, less than 10% of the population resides in states with $m > \ell_c$. Again, this value is in good agreement with our experimental measurement of $\lesssim 10\%$ stabilization. While the excitation energy, static field, and HCP strength approximately match our experimental conditions, the calculated results are not sensitive to small changes in these parameters. As in the single pulse case, higher HCP field strengths result in population transfer to the basis boundary of the calculation which signals the onset of HCP ionization.

V. SUMMARY

We have examined, experimentally and theoretically, transient electric field induced stabilization of Rydberg atoms against AI for three different transient-static field configurations. These time-dependent field configurations mimic the microfields experienced by atoms, molecules, and ions embedded in neutral plasmas or space-charge distributions. We have found that impulsive transients, oriented parallel to relatively weak static electric fields, are totally ineffective in stabilizing atoms against autoionization due to angular momentum mixing in the static field. We predict and observe the stabilization of autoionizing atoms for field configurations where high-m states are populated. These states are stable against autoionization and, in contrast to low-m states, are immune to angular momentum mixing with rapidly autoionizing low-ℓ levels. However, the fraction of atoms that is stabilized is small ($\approx 10\%$ or less) due to the relatively low probability for populating high-m states during a field impulse. Ultimately, impulsive field ionization of the Rydberg electron limits the strength of the transient field that can effectively stabilize the atom against AI or PD. Nevertheless, the use of ultrashort field pulses to stabilize atoms and molecules against AI or PD may prove to be an effective time-resolved probe of state lifetimes and Rydberg electron dynamics in these systems.

ACKNOWLEDGMENTS

We are grateful to E. Wells for stimulating conversations regarding this experiment. This work has been supported by the Packard Foundation and the NSF.

[1] Y. Hahn and K.J. LaGattuta, Phys. Rep. **166**, 195 (1987).
[2] J. Stevefelt, J. Boulmer, and J-F. Delpech, Phys. Rev. A **12**, 1246 (1975).
[3] Y. Hahn *et al.*, in *Recombination of Atomic Ions*, Vol. 296 of *NATO Advanced Studies Institute Series B: Physics*, edited by W. Graham *et al.* (Plenum, New York, 1992).
[4] Y. Hahn, Rep. Prog. Phys. **60**, 691 (1997), and references therein.
[5] T.F. Gallagher, *Rydberg Atoms*, 1st ed. (Cambridge University Press, Cambridge, 1994).
[6] L.D. Landau and E.M. Lifshitz, *Quantum Mechanics (Non Relativistic Theory)*, 3rd ed. (Pergamon Press, Oxford, 1976).
[7] D.S. Belic *et al.*, Phys. Rev. Lett. **50**, 339 (1983).
[8] I. Nasser and Y. Hahn, Phys. Rev. A **30**, 1558 (1984).
[9] H. Gao *et al.*, Phys. Rev. Lett. **75**, 4381 (1995).
[10] R.R. Jones and T.F. Gallagher, Phys. Rev. A **38**, 2846 (1988).
[11] H.A. Bethe and E.E. Salpeter, *Quantum Mechanics of One and Two Electron Atoms* (Springer-Verlag, New York, 1977).
[12] V.L. Jacobs *et al.*, Phys. Rev. Lett. **37**, 1390 (1976).
[13] R.R. Jones and T.F. Gallagher, Phys. Rev. A **39**, 4583 (1989).
[14] W. Sandner, K.A. Safinya, and T.F. Gallagher, Phys. Rev. A **33**, 1008 (1986).
[15] V.L. Jacobs and J. Davis, Phys. Rev. A **19**, 776 (1979).
[16] Due to the quantum defects of the lowest-ℓ states in nonhydrogenic systems, a finite electric field is required to uniformly mix the low angular-momentum character into the Stark levels. To a good approximation, low-ℓ character is uniformly mixed throughout a manifold of Stark states when the energy shift of the most extreme low-m Stark state, $\Delta E_{max} \approx 3/2Fn^2$, exceeds the zero-field energy splitting, $\Delta E_\ell = \delta/n^3$ of the ℓ state with the largest quantum defect δ (modulo 1). This occurs at a field, $F \approx 2\delta/(3n^5)$ [5].
[17] K. LaGattuta, I. Nasser, and Y. Hahn, Phys. Rev. A **33**, 2782 (1986).
[18] K. LaGattuta, I. Nasser, and Y. Hahn, J. Phys. B **20**, 1565 (1987).
[19] A. Muller *et al.*, Phys. Rev. A **36**, 599 (1987).
[20] J.G. Story, B.J. Lyons, and T.F. Gallagher, Phys. Rev. A **51**, 2156 (1995).
[21] Lung Ko, V. Klimenko, and T.F. Gallagher, Phys. Rev. A **59**, 2126 (1999).
[22] V. Klimenko, Lung Ko, and T.F. Gallagher, Phys. Rev. Lett. **83**, 3808 (1999).
[23] F. Robicheaux and M.S. Pindzola, Phys. Rev. Lett. **79**, 2237 (1997).
[24] V. Klimenko and T.F. Gallagher, Phys. Rev. Lett. **85**, 3357 (2000).

[25] R.R. Jones, P. Fu, and T.F. Gallagher, J. Chem. Phys. **106**, 3578 (1997).
[26] A. Burgess, Astrophys. J. **139**, 776 (1964).
[27] E.W. Schlag, *ZEKE Spectroscopy* (Cambridge University Press, Cambridge, 1998), and references therein.
[28] F. Merkt and R.N. Zare, J. Chem. Phys. **101**, 3495 (1994).
[29] M.J.J. Vrakking and Y.T. Lee, J. Chem. Phys. **102**, 8818 (1995).
[30] M.J.J. Vrakking and Y.T. Lee, J. Chem. Phys. **102**, 8833 (1995).
[31] M.J.J. Vrakking, I. Fischer, D.M. Villeneuve, and A. Stolow, J. Chem. Phys. **103**, 4538 (1995).
[32] M.J.J. Vrakking, D.M. Villeneuve, and A. Stolow, Phys. Rev. A **54**, R37 (1996).
[33] P. Bellomo, D. Farrelly, and T. Uzer, J. Chem. Phys. **107**, 2499 (1997).
[34] P. Bellomo, D. Farrelly, and T. Uzer, J. Chem. Phys. **108**, 5295 (1998).
[35] S.R. Proctor, M.J. Webb, and T.P. Softley, Faraday Discuss. **115**, 277 (2000).
[36] N.E. Tielking and R.R. Jones, Phys. Rev. A **52**, 1371 (1995).
[37] J.G. Story, D.I. Duncan, and T.F. Gallagher, Phys. Rev. Lett. **70**, 3012 (1993).
[38] J.E. Thoma and R.R. Jones, Phys. Rev. Lett. **83**, 516 (1999).
[39] S.N. Pisharody and R.R. Jones, Phys. Rev. A **65**, 033418 (2002).
[40] W.E. Cooke, T.F. Gallagher, S.A. Edelstein, and R.M. Hill, Phys. Rev. Lett. **40**, 178 (1978).
[41] M.B. Campbell, T.J. Bensky, and R.R. Jones, Opt. Express **1**, 197 (1997).
[42] R.R. Jones, Phys. Rev. A, **58**, 2608 (1998).
[43] D. You *et al.*, Opt. Lett. **18**, 290 (1993).
[44] R.R. Jones, D. You, and P.H. Bucksbaum, Phys. Rev. Lett. **70**, 1236 (1993).
[45] N.E. Tielking, T.J. Bensky, and R.R. Jones, Phys. Rev. A **51**, 3370 (1995).
[46] T.J. Bensky, G. Haeffler, and R.R. Jones, Phys. Rev. Lett. **79**, 2018 (1997).
[47] J.G. Story, D.I. Duncan, and T.F. Gallagher, Phys. Rev. Lett. **71**, 3431 (1993).
[48] R.R. Jones, Phys. Rev. Lett. **76**, 3927 (1996).
[49] Technically, spontaneous emission from the $4p^+$ to the $3d^+$ ionic level would also lead to the production of a $3dn\ell$, $\ell > \ell_c$ autoionizing level. However, the AI lifetime of such a state should be exceedingly long and, therefore, few if any ions are expected from this mechanism during the 500 nsec duration of the experiment.
[50] M.L. Zimmerman *et al.*, Phys. Rev. A **20**, 2251 (1979).
[51] A. ten Wolde *et al.*, Phys. Rev. A **40**, 485 (1989).
[52] L.D. Noordam *et al.*, Phys. Rev. A **40**, 6999 (1989).
[53] M.B. Campbell, T.J. Bensky, and R.R. Jones, Phys. Rev. A **59**, R4117 (1999).